RSC Advances

ROYAL SOCIETY
OF CHEMISTRY

RSC Advances

High yield multispectral upconversion emission in $Y_2Te_4O_{11}$:Er:Yb nanocrystals on green and NIR excitations

Y. Dwivedi,[a] and S. B. Rai[b]

Detailed synthesis, structural, thermal and radiative properties of Er and Er:Yb codoped $Y_2Te_4O_{11}$ nanocrystals were discussed. Nanocrystals were synthesized by solid state method and reported to emit bright emissions in the wide range of blue-IR regions on excitation with 266 nm, 532 and 808 nm laser radiations via two photon absorption processes. We have reported rarely observed ~711 nm peak on 266 and 532 nm excitations. The emission intensity increases to a great extent in annealed samples and explain on the basis of crystal structure. Judd-Ofelt theory has been employed to estimate the several radiative parameters and effect of structural modifications due to annealing. Emission intensity was found to reduce in presence of Yb^{3+} ions which is suggested due to backward energy transfer from Er → Yb ions. Power dependence and time resolve spectroscopic techniques were used to explore excitation and emission dynamics. These studies clearly indicate promising and futuristic applications of such material for optical fibers and luminescent devices.

1. Introduction

Growing commercial interest in lanthanide (Ln) doped materials induce researchers to develop novel materials and optimize their various physical, optical, magnetic and electrical properties [1, 2]. Erbium (Er) is reported to be one of the most promising elements, among lanthanides, as it provide vast applications in variety of fields, including lasers, telecommunication, fluorescent markers, sensors etc. [3,4]. Er is enriched by superior optical characteristics as its several low energy levels ($^4I_{15/2}$, $^4I_{13/2}$ etc.) possesses long decay time (~milliseconds) that facilitate absorption of another photon incident in mean time. However, spectroscopic properties

of trivalent Er ion are function of host matrix, synthesis condition, nanostructure, codoped ion, excitation wavelengths etc. To optimize Er ion properties for specific application it is necessary to search new host materials, suitable sensitizer ions etc. Till now, optical properties of Er ion are reported in variety of hosts e.g. glass, ceramics, phosphor, polymers [5, 6]. Several combination of lanthanide ions were tested with Er ion e.g. Er:Ce, Er:Sm, Er:Yb, Er:Eu, Er:Tm, etc. however in some of the cases it promote the emission intensity while in few Er ion emission quenches [7,8].

Less studied Yttrium Tellurate host not only offers least stressful lanthanide substitution but also provide virtue of lower lattice vibration that helps to hindered nonradiative relaxations. Detail information about the crystal structures of lanthanum and Ytterbium tellurates were reported by Tromel *et al* [9]. Recently,

a. *Physics Department, National Institute of Technology, Kurukshetra, 136119 Haryana INDIA yashjidwivedi@gmail.com; Tel / Fax. 91-1744-233-503*
b. *Laser and Spectroscopy Laboratory, Department of Physics, Banaras Hindu University, Varanasi- 221005, U.P., INDIA*

Schleid and co-workers have described the synthesis and the crystal structure of Gd_2TeO_6 and Y_2TeO_6 [10, 11]. Previously, bright multicolour upconversion emission has been reported in $Y_2Te_4O_{11}$ phosphor codoped with Er and Yb ions. [12]

In the present article, we report two photon frequency upconversion and downconversion properties of Er doped in Yttrium Tellurate nanocrystals synthesized by solid state reaction method. In addition to this we also attempt to understand the effect of Yb ion codoping which was found to be quenches Er^{3+} ion emission on 532 nm and 808 nm excitations. Detail of the experiments and results obtained are discussed in this article.

2. Experimental

Sample synthesis has been carried out following the solid state reaction protocol. Detail about the sample synthesis can find elsewhere. [12] The commercial high purity ingredients Al_2O_3, Y_2O_3, TeO_2, Yb_2O_3 and Er_2O_3 powders with 99.99% purity were thoroughly mixed to yield the desired stoichiometry of the final powders. The concentration of Er_2O_3 was varied as 0.0, 0.5, 1.0 mol % and while Yb_2O_3 as 0.0, 3, 4, 6 mol %. Mixtures were heated at 1100 ^{o}C for 30 minutes in a computer controlled furnace followed by precalcined at 150 ^{0}C for 5 hours to remove hydroxyl group. Heated material was again crushed and dry pressed to make pellet. The pellets were heated at transition (550 ^{o}C) and crystallization (850 ^{o}C) temperatures (heating rate 2.5^{o}C/min) for one hour to obtain different crystalline phases.

In order to obtain the characteristic transition, crystallization and melting temperatures differential thermal analysis (DTA) and Thermogravimetric analysis (TGA) of the samples were carried out on Regaku Thermoplus Analyzer (DSC8270). X-ray diffraction (XRD) patterns of the samples was recorded using Cu, K_α radiation (λ=0.15406 nm) from a RINT-D/max 2200 H/PC (Rigaku,

Japan) x-ray diffractometer. Data from the International Centre for Diffraction Data (ICDD) sheets were used for the identification of the crystallized phases. UV-NIR reflectance spectra were recorded using a JASCO V-670 absorption spectrophotometer. Absorption coefficient (α) was measured using Kubelka–Munk relation [13] $k/s=(1-R)^2/(1-R)$ where k is the absorption coefficient, s the scattering coefficient, and R represents the absolute reflectance. The pellet thickness was keep >1 mm so no any transmission was possible through the pellet. Scattering coefficient was calculated using Mie-based Monte Carlo simulation method. Refractive index of the samples was estimated using Dimitrov and Sakka method [14]. Photoluminescence measurements were carried out using NIR- 808 nm diode lasers and Green 532 nm (Spitlight 600, Innolas, Germany) Nd:YAG excitation sources and detected by iHR320 (Horiba Jobin Yvon) spectrometer equipped with a R928P photon counting photomultiplier tube (model no. 1424 M) and Synapse CCD (Horiba Jobin Yvon). Photoluminescence decay measurements were carried out with second harmonic pulses at 532 nm from Nd:YAG laser (~7 ns) as an excitation source. The collected signal was fed to 150 MHz digital oscilloscope (model no. HM 1507 of Hameg Instruments) and the decay curves were obtained were used for further calculations. Lifetime of the radiative levels was estimated by fitting the decay curve in an exponential function.

3. Results and discussion

3.1 Thermal and phase analysis

Differential thermal analysis for the as-synthesized and the annealed samples are shown in the Fig. 1. We have marked four exothermic peaks for as-synthesized sample at 715 (Tc_1), 800 (Tc_2), 855 (Tc_3) and 876 ^{o}C (Tc_4) on the other hand in case of annealed sample at 550 ^{o}C/1h, only three peaks at Tc_1= 715 ^{o}C, Tc_2= 800 ^{o}C,

$Tc_3=850$ ^oC and the fourth one Tc_4 is dissolved. Further for the sample annealed at 850 ^oC, $Tc_2= 800$ ^oC is also dissolved and a melting is observed at 874 ^oC. X-ray analysis of as synthesized and annealed samples was carried out in the range of 20-80° angle. Fig. 1 shows the X-ray diffraction patterns of 0.5Er:3Yb codoped as-synthesized and annealed samples. It can be concluded that the as-synthesized sample is basically polycrystalline nature exhibiting several sharp peaks corresponding to atleast three phases of Y-Te-O combination. While annealing at 850 ^oC induces predominant growth of $Y_2Te_4O_{11}$ phase having mean crystalline size of ~60 nm. We have also noted presence of another minor phase, which is assigned to be Al_2O_6Te. However, presence of this phase may not expected to affect much the optical properties of doped ion as substitution of doped ion, in this phase, is practically inaccessible due to large mismatch in ionic radius and charge imbalance.
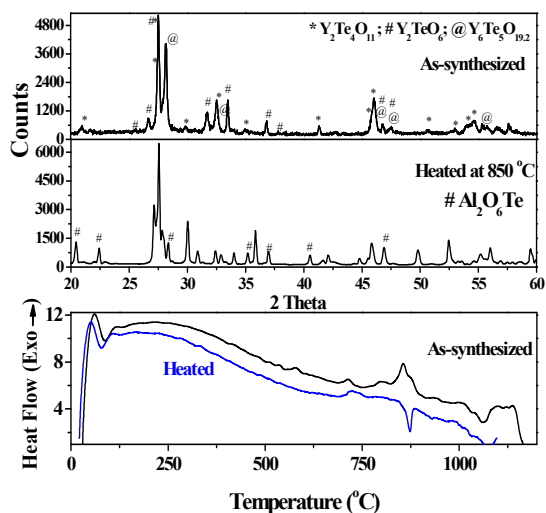
Figure 1. (UP) XRD and (down) Differential Thermal Analysis curves of as-synthesized and heated sample at 850 ^oC.

3.2 Absorption and Judd-Ofelt analysis

It was expected that the annealing at crystallization temperature should bring molecular rearrangements which may be probed by electronic absorption spectroscopy. We have monitored linear absorption spectra of synthesized and processed samples (850 ^oC/1 h) in the spectral range of 200–1800 nm. (Fig. 2) Several sharp absorption peaks corresponding to the intraconfigurational transitions of Er^{3+} and Yb^{3+} ions were identified while an intense broad band, at 250 nm is ascribed due to the charge transfer from ligand oxygen (O^{2-}) to the Er^{3+} ion. [15] It was also noted that the absorption intensity of the peaks were increased in annealed sample.
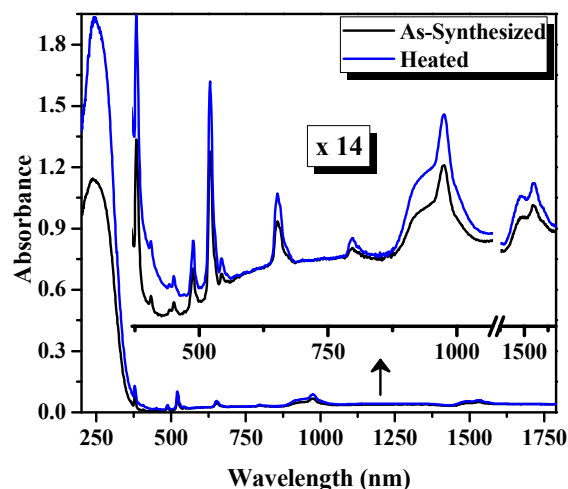
Figure 2. UV-NIR absorption spectra of as-synthesized and heated @850 ^oC samples codoped 0.5Er and 3Yb samples. Enlarge portion of spectra, in the range of 360-1600 nm, is given in inset for the clarity of the peaks.

With the help of absorption spectra, experimental oscillator strengths, of doped rare earth (RE) ions, for precursor and for the annealed sample were obtained using relation mention in ref. [16] Knowing value of experimental and theoretical oscillator strengths, Judd–Ofelt (J-O) intensity parameters $\Omega_{2,4,6}$ can estimate following the relation given in ref. [17] Detail experimental and theoretical oscillator strengths for different transitions in as-

synthesized and annealed samples are compared in Table 1. A measure of the accuracy of the fit between the experimental and calculated oscillator strengths is given by the root mean square (rms) deviation $\sigma_{rms} = \left[\dfrac{\sum (f_{exp} - f_{cal})^2}{N} \right]^{1/2}$ where N is the number of levels included in the fit. The small rms deviation indicates a better fit between the experimental and the theoretical oscillator strengths. In our case it is found to be $0\pm0.12 \times 10^{-6}$. Value of Judd-Ofelt parameters were evaluated by least-square fit program to yield the best fit with theoretical oscillator strengths which gives the best fit to the experimental values. Judd–Ofelt intensity parameters for Er^{3+} in different hosts are shown in Table 2.

The J-O model basically describes the perturbation of the $4f^n$ states by opposite parity $4f^{n-1} 5d$ on the basis of three parameters $\Omega_{\lambda=2,4,6}$ [18-20]. Since the admixing of the $4f^n$ states in RE ion is the function of local crystal field, symmetry, bonding nature etc, J-O parameters in turn yield information about the local interactions of RE^{3+} with the surrounding environment. According to J-O theory, Ω_2 is sensitive to the environmental configuration symmetry of rare-earth ions, while Ω_4 and Ω_6 related to the rigidity of host. [21] In our calculation the value of Ω_4 is found negative. Since a negative value for any J-O coefficients is not consistent with the theory and it did not stand theoretical meaning it was assumed to be zero. [22] For as-synthesized and annealed samples, the Ω_λ (λ= 2, 4 and 6) parameters follow the similar trend i.e. $\Omega_2 > \Omega_6 > \Omega_4$. The larger value of Ω_2 for annealed sample reveals that the Ω_2 parameter increases by increasing the volume fraction of $Y_2Te_4O_{11}$ nanocrystals. It is well known that the Ω parameters, especially the Ω_2, depend on the asymmetry and covalence of RE ion sites in host i.e. value of Ω_2 increases with increasing site distortion of RE ions and with increasing covalent character of RE–O bonds. A larger value of Ω_2 in

heated sample shows a larger asymmetry in comparison to as-synthesized sample. It is observed that in the case of as-synthesized sample $Y_2Te_4O_{11}$ monoclinic crystals are in minor proportion and possessed lower symmetry in comparison to the crystals $Y_6Te_5O_{19.2}$ (Cubic) and Y_2TeO_6 (Orthorhombic) in major proportion, while annealed sample was dominated by $Y_2Te_4O_{11}$ crystals. The slight change in Ω_2 is expected due to the lower symmetrical microenvironment around Er and Yb ions. It is anticipated that the increase in the covalence of Er–O bond contribute to the increase in the value of Ω_2. Parameter Ω_6 is a measure of rigidity of the medium [23], which is related to the mean force constant of the RE-O bond. In our calculation, the value of Ω_6 parameter increases which shows higher force constant consequently stronger band strength (RE-O) in the annealed sample. To monitor the effect of heating on the bonding characteristics Nephelauxetic ratio (β) was calculated for as-synthesized and annealed samples (Table 1). The bonding nature of the ion in host environment can evaluate from bonding parameter using relation: $\delta = \dfrac{1-\beta}{\beta}$. Although the sign of bonding parameter is found to be negative in both the cases (as-synthesized and annealed), the value of δ is either similar or slightly more negative for the annealed sample. The calculated J-O coefficients were further used to evaluate the various radiative properties (spontaneous emission probability, transition probability, radiative lifetime etc) of the doped RE ions. These parameters may be calculated using relations mentioned in ref. [17] and the values thus obtained are tabulated in Table 3.

3.3 Photoluminescence analysis

3.3.1 532 nm excitation

Energy level positions in Er^{3+} ions are favorable for upconversion emission on excitation with 532 nm (~18,800 cm^{-1}) laser radiation. Emission spectra of the Er doped as-synthesized and annealed (850 ^{o}C/1 h) samples were recorded, in the range of 350 – 2100 nm, on excitation of 532 nm laser radiations and the spectra thus obtained are shown in Fig. 3.
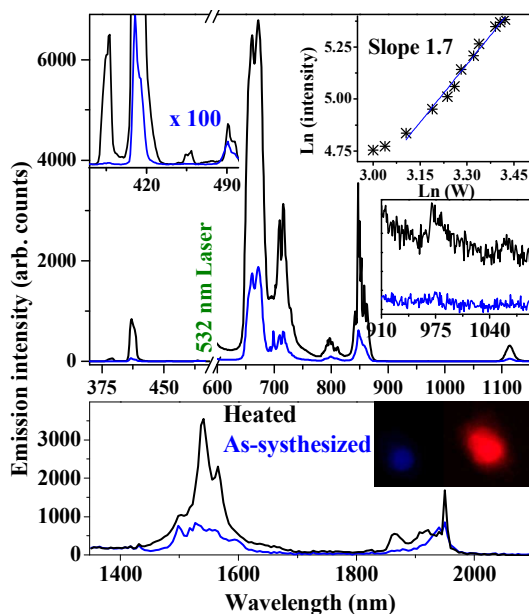
Figure 3: Down and Upconversion spectra of 0.5 Er doped as-synthesized and annealed samples on 532 nm excitation. Inset figure shows the enlarge portion of the spectra, and power dependent ln-ln plot for 389 nm ($^4G_{11/2} \rightarrow {}^4I_{15/2}$) of the heated sample on 532 nm excitations. Camera image of emission, using blue and red filters are also given in inset.

The emission spectrum of as-synthesized sample exhibits weak peaks in blue region at 389, 410, 454 and 491 nm arise due to $^4G_{11/2}$; $^2H_{9/2}$; $^2F_{5/2}$; and $^4F_{7/2} \rightarrow {}^4I_{15/2}$ transitions respectively. The green emissions cannot observe since it overlaps with the laser radiation. However, red (670 nm, 711 nm, 800 nm due to $^4F_{9/2} \rightarrow {}^4I_{15/2}$, $^4F_{7/2} \rightarrow {}^4I_{13/2}$, $^4I_{9/2} \rightarrow {}^4I_{15/2}$; 852, 860 nm due to $^2H_{11/2}$, $^4S_{3/2} \rightarrow {}^4I_{13/2}$ transitions) and NIR (975 and 1113 nm due to $^4I_{11/2} \rightarrow {}^4I_{15/2}$, and

$^4F_{9/2} \rightarrow {}^4I_{13/2}$ transitions) peaks are observed. Whereas sample annealed at 850 ^{o}C/1h shows intense blue upconversion and red/NIR downconversion emissions. Integrated area of the peaks at 389 and 670 nm is 05 and 03 times larger than in the case of as-synthesized sample. In addition to peaks observed in visible region, infrared peaks at 1.5 and 1.9 micrometer is also observed corresponding to $^4I_{13/2} \rightarrow {}^4I_{15/2}$ and $^4I_{9/2} \rightarrow {}^4I_{13/2}$ transitions, respectively.

The observed emission spectrum can be understood on the basis of two photon absorption process i.e. excited state photon absorption followed by ground state photon absorption. Er^{3+} ion contains two levels $^2H_{11/2}$ and $^4S_{3/2}$ in green region located at ~19,200 cm^{-1} and ~18,350 cm^{-1}, respectively. These levels are supposed to be thermally coupled at room temperature as separation between these levels is only ~900 cm^{-1}. Initially, 532 nm laser photon is absorbed in the ground state ($^4I_{15/2}$) of Er^{3+} and the ions are promoted to the $^2H_{11/2}$ state. Ions in $^2H_{11/2}$ relax to $^4S_{3/2}$ state via non-radiative relaxation process. Due to longer lifetime of these levels (~order of 10^2 μs), it is possible that a 532 nm laser photon may absorbed by the excited ions in this state and promoted to $^4G_{9/2}$ state however, we didn't observed any peak in UV region (< 389 nm). The observed upconversion emissions are due to the absorption of 532 nm laser photons and consequently, radiative transitions to the lower states. [Fig. 4].
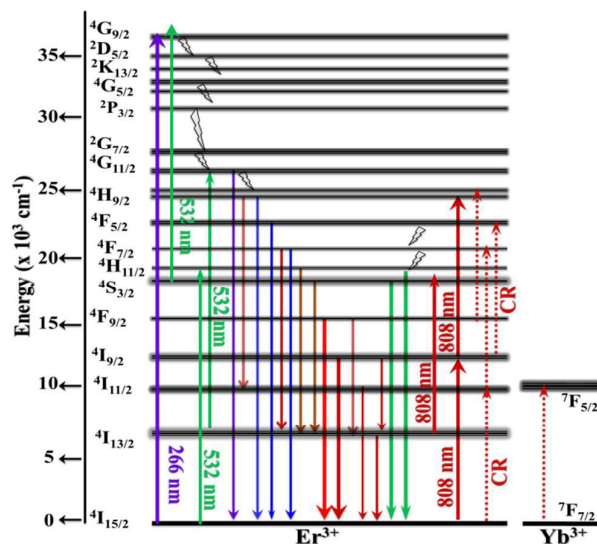
Figure 4. Energy level diagram of Er and Yb ions showing excitation, and the possible up and down conversion pathways. Dotted lines represent the possible cross-relaxation (CR) pathways.

It was also noted that enhancement in infrared region didn't improved much in comparison to visible region, which can understand on the basis of excited state absorption from $^4I_{13/2}$ level (lifetime ~3 ms) also which ultimately reduce population in $^4I_{13/2}$ level and promote ions in $^4G_{11/2}$ level and improve emission at ~389 nm.

For better understanding of the population building mechanism through two photon absorption process, the upconversion emission intensity of the blue (389 nm) emission as a function of the excitation power has been studied using relationship between the emission intensity I_{em} and the excitation intensity I_{ex} is as follows: $I_{em} = K (I_{ex})^n$. Thus, a plot of log (I_{em}) versus log (I_{ex}) should yield a straight line with slope n. The log-log plot of upconversion luminescence intensity as a function of pump power for the codoped sample is depicted in Fig. 3. It is observed that the emission intensity of blue emission increases linearly with excitation

power and the linear fitting of the curve indicate the involvement of two photons (~ 1.7) for the emission process.

To verify our concept of two photon absorption, we have monitored the emission spectrum of the 0.5 mol% Er doped sample on 532 nm and 266 nm laser excitations with identical laser power (see Fig. 5). We have observed that the peak positions were identical however the intensity of the peaks was not same in both the excitations. It is evident that on 266 nm excitation, intensity of peaks in blue regions i.e. 389, 410, 454 and 491 nm are much weaker than the peak intensity on 532 nm excitation. In contrast, peaks in red regions are brighter on 266 nm than the 532 nm. The observed variation in peak intensity is expected due to the involvement of another pumping channel i.e. resonant excitation of 532 nm photon through $^4I_{13/2} \rightarrow {}^4G_{11/2}$ transition which enhances the emission intensity in blue regions. This additional pumping channel is not available on 266 nm excitation [24].
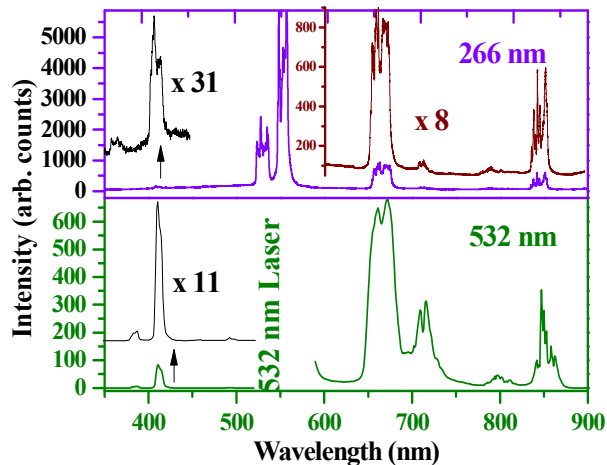
Figure 5. Comparison between the emission patterns on 266 nm and 532 nm excitation of 0.5Er sample (850 °C/1 h). Selected portions of the spectrum are enlarged for clarity of the emission peaks.

One interesting observation in the spectra of Er doped samples on excitation with 266 nm, 532 nm and ~980 nm, 808 nm, 797 nm, 325 nm [24, 25] is the occurrence of bright peak centered at 711 nm. Peak at 711 nm was not reported so far, on the basis of open literature available. Since Er ion does not possess any energy level at 711 nm (~1400 cm^{-1}) hence observation of this peak is only due to excited – excited state absorption process. Energy of this transition is matches well with the energy of $^2H_{9/2} \rightarrow ^4I_{11/2}$ and $^4F_{7/2} \rightarrow ^4I_{13/2}$ transitions. The peak ratio of 670 nm to 710 nm is also varied dramatically on 266 nm and 532 nm excitations. In case of 532 nm excitation peaks intensity ratio of $^4F_{9/2} \rightarrow ^4I_{15/2}$ (670 nm) to $^4F_{7/2} \rightarrow ^4I_{13/2}$ (710 nm) transitions was found to increase 09 multiple than the 266 nm excitation. The observed variation is due to the additional pumping channel through $^4I_{13/2} \rightarrow ^4G_{11/2}$ transition while exciting with 532 nm.

To monitor the effect of codoping of trivalent Yb ions, we have doped different concentrations of Yb ions with 0.5 mole % Er ions in the host and excite with 532 nm radiation (see Fig. 6).

This is to be noted that the trivalent Yb ions are practically transparent to 532 nm laser photons since it do not possess any energy levels at ~18,800 cm^{-1} (~532 nm) hence expected to be neutral. However, when a trace amount of Yb is also present, the emission intensity of Er ion reduces considerably. Peak at 670 nm reduced to 5.5 and 9 multiple in 3 and 6 mol% Yb codoped samples. It is to be noted that the XRD patterns didn't show any major change in crystalline structure atleast upto 6 mol% Yb concentrations. It was reported previously that the emission intensity of the lanthanide ions are the function of pump power, ion concentration, lifetime of the intermediate states and several other parameters. Er^{3+} ion is rich of dense energy levels and energy difference of several levels is partially overlapped with the energy difference of Yb^{3+} ions viz. These transitions endorse to depopulate Er^{3+} ions through cross-relaxation processes: Er ($^2H_{11/2}$, $^4S_{3/2}$; $^2H_{9/2}$; $^4F_{9/2}$; $^2H_{9/2}$) + Yb ($^2F_{7/2}$); $\rightarrow$ Er ($^4I_{11/2}$; $^4I_{13/2}$; $^4S_{3/2}$; $^4G_{11/2}$) + Yb ($^2F_{5/2}$). It is expected that the energy absorbed in Yb^{3+} ions relaxed through nonradiative rapid multiphonon relaxation process via defect sites, since no enhancement at ~10,000 cm^{-1} is observed.

To explore the complex emission dynamics of Er^{3+} ion on 532 nm excitation, we have recorded the decay curves of $^4F_{9/2} \rightarrow ^4I_{15/2}$ (670 nm) transition and depicted in Fig. 7.

Figure 6. Comparison between the PL spectra of 0.5 Er and 0.5 Er: 3, 6 Yb doped annealed samples on 532 nm excitation.
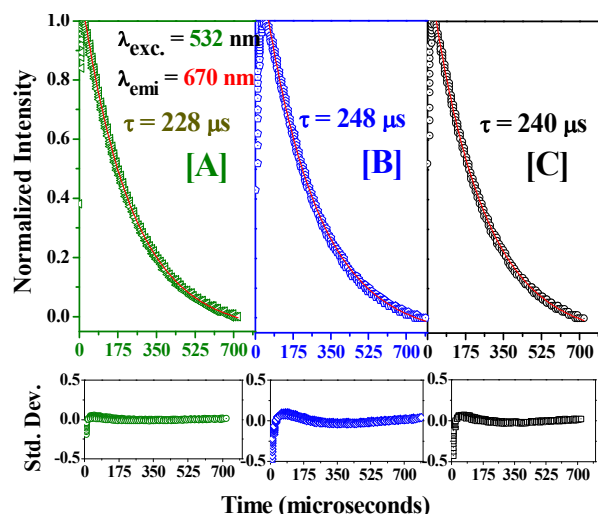
Figure 7. Decay curves corresponding to the $^4F_{9/2} \rightarrow {}^4I_{15/2}$ (670 nm) transition of [A] as-synthesized, [B] annealed 0.5 Er doped sample and [C] 3 Yb codoped annealed sample on excitation with pulsed (~7 ns) 532 nm.

At higher concentration of ions, non-radiative relaxation energy transfer process come into play, so the curve fitting with an exponential function may not give an accurate lifetime value. Hence, only a mean value of lifetime and an effective relaxation rate may calculate. We have calculated effective decay time using following relation: $\tau^{eff} = \dfrac{\int_0^\infty I(t)dt}{I(0)dt}$ where I (t) represent, emission intensity at time t after incident beam was completely cutoff.

The decay curve of as-synthesized sample was found to be mono-exponential and the lifetime value estimated to be 228 μs. However, when sample was heated at 850 °C/ 1 h radiative lifetime was found to increase and estimated to be 248 μs. The observed increment in radiative lifetime is due to the transformation of polycrystalline to single crystalline nature of the material. The radiative lifetime slightly reduces (~240 μs) when 3 mol % of Yb ions

are also codoped. The observed reduction in lifetime is due to the existence of energy bypass channel through cross-relaxation process Er ($^4F_{9/2}$) + Yb ($^2F_{7/2}$); → Er ($^4I_{13/2}$) + Yb ($^2F_{5/2}$) when Yb is also present in the host. The cross relaxation rate W_{CR} can be estimated from following relation:

$$W_{CR} = \frac{1}{\tau^{eff}[^4F_{9/2}](0.5Er:3Yb)} - \frac{1}{\tau^{eff}[^4F_{9/2}](0.5Er)}$$

The value of W_{CR} was found to be 135 s^{-1}, which verify an efficient cross-relaxation energy transfer process from Er to Yb ion.

3.3.2 808 nm excitation

The emission spectra of Er^{3+} doped samples, on excitation with 808 nm laser radiation, are shown in Fig. 8. Spectra exhibit three major peaks: two, bright green, peaks centered at 525 and 555 nm and a broad peak, in red region, centered at 670 nm. The emission intensity of the bands is however smaller compared to the 266 nm and 532 nm excitations. On excitation with 808 nm photon, the $^4I_{9/2}$ level of Er^{3+} and thereafter $^4I_{11/2}$ and $^4I_{13/2}$ levels are populated by non-radiative relaxation process. The excited Er^{3+} ions in the $^4I_{11/2}$ and $^4I_{13/2}$ level reabsorb 808 nm photons and are promoted to $^4S_{3/2}$, $^2H_{11/2}$ and $^4F_{9/2}$ levels to give emission at 525, 555 and 670 nm. The detail absorption process is given in Fig. 4.
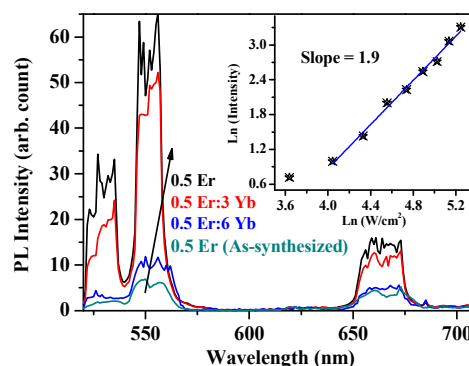
Figure 8. Upconversion emission spectra of 0.5 Er (as-synthesized and annealed), 0.5 Er : 3 Yb and 0.5 Er : 6 Yb (annealed) samples on

808 nm excitations. Inset figure shows the power dependence ln-ln plot for 555 nm emission.

Yb^{3+} ions do not absorb 808 nm radiations and no emission appears from it, in singly doped Yb ion. An interesting thing observed on 808 nm excitation when Yb^{3+} is also present with Er^{3+} the intensity of the green and red emissions reduces. The excited Er^{3+} ions relax from $^4I_{9/2}$ level to $^4I_{11/2}$ and $^4I_{13/2}$ levels. Energy of $^4I_{11/2}$ level is similar to the $^2F_{5/2}$ level of Yb^{3+} ion. It seems that the energy migrates from Er^{3+} ions to Yb^{3+} ions. This reduces the population of $^4I_{11/2}$ level and thereby the upconversion process in Er^{3+} ion. Thus the intensity of green and red bands of Er^{3+} ion is reduced. Thus Yb^{3+} in the case of 808 nm excitation acts as quencher. Observed reduction in optical intensity, in presence of Yb ion, has been observed earlier also by us [7].

4. Conclusions

In summary, Er-doped and Er:Yb co-doped $Y_2Te_4O_{11}$ materials has synthesized using solid state reaction method. Various structural, thermal and optical properties of the materials were explored. Absorption spectra of the as-synthesized and annealed samples were recorded and Judd-Ofelt intensity parameters and various radiative parameters were calculated and compared. These calculations reveal higher cross-sections in the annealed sample. Detailed Stokes and anti-Stokes emissions were investigated using 266 nm, 532 nm and 808 nm laser radiations. When the samples were excited with 532, and 808 nm lasers, they yield emission pattern in UV-Vis-IR regions through two photon absorption. Among them green emission was the most intense one. Emission intensity was found to reduce on addition of trace amount of Yb ions.

Acknowledgment

References

1.   G. Wang, Q. Peng, and Y. Li, *Acc. Chem. Res*. 2011, **44**, 322.

2.   C. Bouzigues, T. Gacoin, and A. Alexandrou, *ACS Nano* 2011, **5**, 8488.

3.   (Eds) S. B. Rai, and Y. Dwivedi Synthesis, Characterization and Applications of Multifunctional Materials, Nova Science Publishers, USA, 2012.

4.   M. Nichkova, D. Dosev, R. Perron, S. J. Gee, B. D. Hammock, and I. M. Kennedy, *Anal. Bioanal. Chem*. 2006, **384**, 631.

5.   (a) B. S. Cao, J. L. Wu, X. H. Wang, Y. Y. He, Z. Q. Feng, B. Dong, and L. Rino, *AIP Advances* 2015, **5** 087136 (b) B. Dong, B. Cao, Y. He, Z. Liu, Z. Li, and Z. Feng, *Adv. Mater.* 2012, **24,** 1987-1993.

6.   H. Zhu, D. Tang, Y. Duan, and D. Luo, J. Zhang, *Opt Express*, 2013, **21**, 26955.

7.   Y.Dwivedi, A. Rai, and S.B.Rai, *J. Lumin.* 2009, **129,***629.*

8.   A. Bahadur, Y. Dwivedi, and S.B.Rai *Spectrochim Acta A* 2010, **77**, 101.

9.   M. Tromel, F. W. Hutzler, H. G. Burckhardt, C. Platte, and E. Munch, *Z. Anorg. Gllg. Chem* 1987, **551**, 95.

10. S. F. Meier, and T. Schleid, *J. Sol. State Chem.* 2003, **171**, 408.

11. P. Hoss, and T. Schleid, *Acta Cryst E* 2007, **63**, i133.

12. Y. Dwivedi, K. Mishra, and S. B. Rai, *J. Alloys Compd* 2013, **572**, 90.

13. P. Kubelka, and F. Munk, *Z Tech. Phys. (Leipzig)* 1931,**12,** 593.

14. B. Eraiah, *Bull. Mater. Sci.* 2010, **33**, 391.

15. X. Zhou, L. Zhao, Q. Feng, X. Wei, and C. Duan, *Mater. Res. Bull.* 2009, **44,** 1935.

16. (Eds) C. G. Walrand, and K. Binnemans, Handbook on the Physics and Chemistry of Rare Earths, Amsterdam, 1998.

17. G. Kaur, Y. Dwivedi, and S.B. Rai, *Opt. Comm.* 2010, **283**, 3441.

18. B. R. Judd, *Phys. Rev.* 1962, **127**, 750.

19. G. S. Ofelt, *J. Chem. Phys.* 1962, **37,** 511.

20. A. A. Kaminskii, V. S. Mironov, A. Kornienko, S. N. Bagaev, G. Boulon, A. Brenier, and B. D. Bartolo, *Phys. Status Solidi (a)* 1995, **151**, 231.

21. C. K. Jorgensen, and R. Reisfeld, *J. Less-Common Metals* 1983, **93**, 107.

22. B. E. Bowlby and B. D. Bartolo, *J. Lumin*. 2002, **100**, 131.

23. M. P. Hehlen, N. J. Cockroft, T. R. Gosnell, and A. J. Bruce, *Phys. Rev. B* 1997, **56**, 9302.

24. K. Kumar, S.B. Rai, and D.K. Rai, *J Non-Cryst. Solids* 2007, **353**, 1383.

25. Y. Dwivedi, and S. C. Zilio, *Sci. Adv. Mate.* 2013, **5**, 1514.

26. A. A. Kaminskii, V. S. Mironov, A. Kornienko, S. N. Bagaev, G. Boulon, A. Brenier and B. Di Bartolo, *Phys. Status Solidi (a)* 1995, **151**, 231.

27. A. A. Kaminskii, A. G. Petrosyan, G. A. Denisenko, T. I. Butaeva, V. A. Fedorov, S. E. Sarkisov, *Phys. Status Solidi (A)* 1982, **71**, 291.

28. R. Sosa, I. FÖldvári, A. Watterich, A. Munoz, R. S. Maillard and G. Kugel, *J. Lumin.* 2005, **111**, 25.

Table 1

$^4I_{15/2}{\rightarrow}J`$ Energy (cm^{-1})	As-synthesized sample				Annealed sample			
	Oscillator strength		β	δ	Oscillator strength		β	δ
	Experimental	Theoretical			Experimental	Theoretical		
$^4I_{13/2}$ (~6535)	27.7 – 1.7 (MD)	26	1.0240	-0.0233	32-2.1[MD]	29.3	1.0252	-0.0246
$^4I_{9/2}$ (~12563)	5.00	4.3	1.0041	-0.0041	5.39	4.9	1.0151	-0.0041
$^4F_{9/2}$ (~15361)	4.02	4.0	1.0150	-0.0150	4.77	4.3	1.0053	-0.0150
$^4S_{3/2}$ (~18416)	0.96	0.90	1.0051	-0.0051	1.21	1.02	1.0033	-0.0053
$^2H_{11/2}$ (~19194)	3.05	2.57	1.0010	-0.0010	4.32	3.94	1.0034	-0.0033
$^4F_{7/2}$ (~20492)	0.95	0.89	1.0033	-0.0033	1.45	1.39	1.0023	-0.0034
$^4F_{5/2}$ (~21834)	0.29	0.19	1.0023	-0.0023	0.518	0.481	1.0012	-0.0023
$^4F_{3/2}$ (~22936)	0.172	0.11	1.0012	-0.0012	0.389	0.31	1.0034	-0.0012
$^2H_{9/2}$ (~24570)	0.332	0.293	1.0031	-0.0031	0.864	0.72	1.0029	-0.0034
$^4G_{11/2}$ (~26455)	1.036	1.0	1.0027	-0.0028	1.425	1.26	1.0036	-0.0028
$^4G_{9/2}$ (~27473)	0.284	0.25	1.0035	-0.0035	0.492	0.41	1.0012	-0.0036
$^2P_{3/2}$ (~31348)	0.518	0.481	1.0011	-0.0010	0.734	0.58	1.0011	-0.0010
rms (Δf)=0.12x10^{-6}								

Table 2

Sample	Judd-Ofelt parameters			Ref.
	Ω_2	Ω_4	Ω_6	
As-synthesized	0.47	-1.04	1.49	Present work
Annealed	0.56	-1.12	1.73	Present work
YAlO$_3$	0.95	0.58	0.55	[26]
YAG	0.45	0.98	0.62	[27]
Bi$_2$TeO$_5$	0.698	0.174	0.123	[28]

Table 3

Transitions (energy)	As-synthesized sample			Annealed sample		
	Radiative probability (s^{-1})	Branching ratio (β_R) %	Radiative lifetime (ms)	Radiative probability (s^{-1})	Branching ratio (β_R) %	Radiative lifetime (ms)
$^4I_{13/2} \rightarrow {}^4I_{15/2}$	221	0.0194	4.5	228	0.02	4.4
$^4I_{11/2} \rightarrow {}^4I_{15/2}$	182	0.0160	5.5	193	0.016	5.2
$\rightarrow {}^4I_{13/2}$	22	0.0020	45.5	30	0.0025	33.4
$^4I_{9/2} \rightarrow {}^4I_{15/2}$	232	0.0203	4.3	243	0.0200	4.1
$\rightarrow {}^4I_{13/2}$	26	0.0023	38.5	28	0.0023	35.7
$\rightarrow {}^4I_{11/2}$	2.6	0.0003	385	3.2	0.0003	312.5
$^4F_{9/2} \rightarrow {}^4I_{15/2}$	2140	0.1875	0.467	2213	0.1851	0.452
$\rightarrow {}^4I_{13/2}$	45	0.004	22	48	0.0041	21
$\rightarrow {}^4I_{11/2}$	39.6	0.0035	25	46.2	0.0038	21.6
$\rightarrow {}^4I_{9/2}$	2.1	0.0002	476	2.7	0.0002	370.4
$^4S_{3/2} \rightarrow {}^4I_{15/2}$	1335	0.117	0.75	1496	0.1252	0.67
$\rightarrow {}^4I_{13/2}$	828	0.0725	1.2	863	0.0722	1.2
$\rightarrow {}^4I_{11/2}$	38	0.0033	26.3	42	0.0035	23.8
$\rightarrow {}^4I_{9/2}$	54	0.0047	18.5	62	0.0050	16.1
$\rightarrow {}^4F_{9/2}$	0.8	0.0000	1250	1.2	0.0001	833.4
$^2H_{11/2} \rightarrow {}^4I_{15/2}$	6032	0.5286	0.1658	6212	0.5200	0.161
$\rightarrow {}^4I_{13/2}$	85	0.0074	11.8	92	0.0077	11
$\rightarrow {}^4I_{11/2}$	42	0.0037	23.8	46	0.0039	21.7
$\rightarrow {}^4I_{9/2}$	71	0.0062	14.1	82	0.0069	12.2
$\rightarrow {}^4F_{9/2}$	14	0.0012	71.43	21	0.00175	48
$\rightarrow {}^4S_{3/2}$	0	0	0	0	0	0
Total radiative transition probability (s^{-1})		11411		11951		